Nanoscale

PAPER

View Article Online
View Journal | View Issue

Cite this: *Nanoscale*, 2014, **6**, 12532

Nano/micro-structured Si/CNT/C composite from nano-SiO_2 for high power lithium ion batteries

Xuejiao Feng,[a] Jun Yang,*[a] Yitian Bie,[a] Jiulin Wang,[a] Yanna Nuli[a] and Wei Lu[b]

Received 14th July 2014,
Accepted 4th August 2014

DOI: 10.1039/c4nr03948c

www.rsc.org/nanoscale

Nano/micro-structured pSi and pSi/CNT particles were synthesized from nano-SiO_2 as both a template and silicon precursor *via* a combination of spray drying and magnesiothermic reduction, followed by a nano-layer carbon coating by chemical vapor deposition to obtain a nano/micro-structured pSi/C and pSi/CNT/C composite. In the hierarchical microstructure of the pSi/CNT/C composite, Si nanoparticles less than 20 nm in size were homogenously dispersed in an electronically conductive and porous network of multiwall carbon nanotubes, which can accommodate the volume changes in Si and improve the structural and conductive stability during repeated cycles leading to excellent electrochemical performance. The pSi/CNT/C presented reversible capacities of *ca.* 2100 mA h g^{-1} at 1 A g^{-1} and *ca.* 1370 mA h g^{-1} at a high current rate of 5 A g^{-1}. Its capacity retention after 100 cycles was 95.5% at 1 A g^{-1}.

Introduction

Silicon is a very attractive anode material because of its large theoretical capacity at room temperature ($Li_{15}Si_4$, 3600 mA h g^{-1}) and moderate operating voltage (0.4–0.5 V *vs.* Li/Li^+).[1,2] Nevertheless, current Si based electrodes often show considerably lower capacity than the theoretical value upon cycling and poor rate performance mainly because of the small Li^+ diffusion rate inside the silicon, which poses a kinetic barrier to fully convert silicon to $Li_{15}Si_4$ at a normal charge/discharge rate, especially for large grain silicon.[3–5] Another challenge is the poor cycle stability, which is caused by the drastic volume change during cycling. Extensive research has addressed this issue, typically by constructing porous Si structure or using nanoscaled Si particles to improve the electrochemical performance.[6–10] The advantage of microscaled porous particles over nanosized Si powders (particularly below 100 nm in size) lies in the reduced aggregation tendency, convenient transport and application. The porous structure can provide sufficient space to absorb the large volume expansion.[11–15] Moreover, the penetration of liquid electrolyte into the open porous structure can increase the interfacial area between the electrode and electrolyte, which is favorable for fast Li^+ transport and high rate performance. Various methods, such as chemical/electrochemical etching, and porous templates have been employed for preparing porous silicon. The etching process is mainly applied to convert bulk silicon into a porous structure with tunable pore size and porosity.[16] Mingyuan Ge *et al.*[17] proposed the chemical etching of boron-doped silicon wafers in a $HF/AgNO_3$ solution to prepare porous silicon nanowire, which displayed superior electrochemical performance and long cycle life because an alginate binder was used. The concept of a porous template is to fill up the void space and then etch away the template. Hyunjung Kim *et al.*[18] reported 3D porous bulk Si particles by the thermal annealing and etching of physical composites obtained from butyl-capped Si gels and SiO_2 at high temperature. This material delivered a reversible capacity of 2800 mA h g^{-1} at a rate of 1C after 100 cycles. The cycling improvement benefited from its highly porous and interconnected structure. Our group[7] employed the magnesiothermic reduction of a SBA-15 silica template to obtain 3D mesoporous Si, which displayed a stable capacity of *ca.* 1500 mA h g^{-1} for 100 cycles at 1C and high rate capability up to 15C. However, the practical applications of these porous Si-based materials may be largely impeded by the complicated and expensive approaches.

The development of silicon based materials from cheap raw materials and scalable manufacturing processes is needed urgently.[19] Lanyao Shen *et al.*[20] prepared a porous silicon anode material from magnesiothermically-reduced diatomaceous earth. The silicon source is cheap, but the electrochemical performance of obtained porous silicon/carbon is still unsatisfactory. Yoon Hwa *et al.*[21] prepared mesoporous nanosized Si through the reduction of amorphous SiO_2 with Mg powder under high-energy mechanical milling. It exhibited a capacity larger than 1600 mA h g^{-1} over 30 cycles. Although the raw material of amorphous SiO_2 is cheap, the milling process using 900 rpm may be difficult to scale up.

[a]*School of Chemistry & Chemical Engineering, Shanghai Jiao Tong University, Shanghai, 200240, China. E-mail: yangj723@sjtu.edu.cn*
[b]*Department of Mechanical Engineering, University of Michigan, Ann Arbor, MI 48109, USA*

In addition, the use of a mixed-conducting carbon phase was demonstrated as an another effective way of reducing the volume change. The incorporation of graphite,[22,23] CNT[24] or graphene[25] with silicon can enhance the cycle performance of lithium ion batteries by improving the electronic conductivity and suppressing the volume change in Si active materials. In particular, graphene could be an excellent substrate to accommodate active materials owing to its unique two-dimensional nanostructure with high electronic conductivity, superior mechanical properties, excellent chemical tolerance, and high surface area.[26–28] However, it is still much more expensive than multiwall carbon nanotubes (MWCNTs), another stable conducting and mechanical reinforcer.[29,30] It was reported that the dispersion of MWCNT in silicon electrode could increase the cycling performance.[31] However, it is difficult to disperse MWCNTs into a silicon electrode homogenously and obtain good contact between the MWCNTs and silicon particles. On this issue, direct MWCNT growth on the surface of Si nanoparticles was actualized by a simplified chemical vapor deposition (CVD) method.[32] The well dispersed MWCNT serves as a kind of "electronic wire" and robustly connects Si nanoparticles. Aurélien Gohier *et al.*[33] reported the electrochemical characterization of silicon decorated with vertically aligned carbon nanotubes directly grown onto metal foil *via* a two-step CVD process. Owing to its specific hierarchical hybrid nanostructure, in which 10 nm Si nanoparticles were homogenously deposited on very thin CNTs, 5 nm in diameter, this composite delivered a high reversible Li storage capacity of 3000 mA h g^{-1} at 1.3C.

Inspired by the above-mentioned material designs and aimed at low cost and facile up-scaling production, we conceived and prepared nano/micro-structured silicon materials from commercial cheap nano-SiO_2 raw material through spray drying granulation, reduction of silica by magnesium and HCl etching. Here, single silicon nanoparticles are assembled in micrometre-sized particles with many pores and the addition of the multiwall carbon nanotubes (MWCNTs) not only enhances the electronic conductivity, but also stabilizes the original spherical morphology. The electrochemical performance of the nano/micro-structured composite without/with MWCNT was investigated in detail.

Experimental

Material preparation

Preparation of $pSiO_2$. Commercial nano-SiO_2 (*ca.* 20 nm, Aladdin) (5 g) was added to a 1 wt% aqueous polyvinyl alcohol (PVA, 94.0–96.0% mol/mol, Aladdin) solution. The mixture was then stirred for 2 h at room temperature and then homogenously mixed under ultrasonication. The weight ratio of SiO_2 and PVA was fixed to 1 : 1. A porous composite precursor was made using a spray dryer with a nozzle diameter of 1.4 mm (B-290, BUCHI). In this process (see steps 1 and 2 in route (1) of Scheme 1), the slurry containing SiO_2 and PVA was sprayed at a speed of 5 mL min^{-1}, and the inlet and outlet temperatures were set to 220 °C and 120 °C, respectively. The obtained composite was designated as $pSiO_2$/PVA. The as-made $pSiO_2$/PVA precursor was then heated to 900 °C at a speed of 5 °C min^{-1} and maintained at 900 °C for 2 h in air to remove the PVA binder. Finally, it was cooled to room temperature at 5 °C min^{-1}. The prepared porous SiO_2 particles, mostly in a ball shape, were abbreviated as $pSiO_2$.

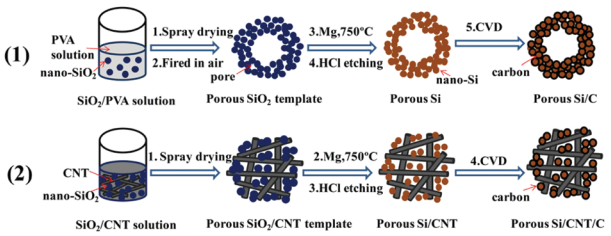

Scheme 1 Schematic for the synthesis routes of the nano/micro-structured pSi/C and pSi/CNT/C composite.

Preparation of $pSiO_2$/CNT. 9 g nano-SiO_2 (*ca.* 20 nm, Aladdin) and 0.22 g MWCNT (OD > 50 nm, length 10–20 μm, purity >95%, Chengdu Organic Chemical Co., Ltd, China) were added to deionized water, the mixture was stirred for 12 h at room temperature and then homogenously mixed under ultrasonication. The nano/micro-structured composite precursor was made by spray dryer with the above mentioned conditions. The obtained composite was designated as $pSiO_2$/CNT.

Magnesiothermic reaction. $pSiO_2$ or $pSiO_2$/CNT and magnesium powder (Sinopharm Chemical Reagent Co. Ltd, 100–200 mesh) were placed in a corundum boat (silica/Mg 1/0.9 in weight), and then heated in a tube furnace at 750 °C for 4 h under Ar (95 vol%)/H_2 (5 vol%) mixed atmosphere. The heating and cooling rates were maintained at 2 °C min^{-1}. The obtained brown powder was first immersed in a HCl solution (25 mL, 2 M) for 12 h, then washed with distilled water by centrifugation 4 times, finally washed with ethanol and vacuum-dried at 80 °C for 3 h. By this process (step 4 in route (1) or step 3 in route (2)), MgO was removed. The materials obtained from the $pSiO_2$ and $pSiO_2$/CNT precursors were abbreviated as pSi and pSi/CNT, respectively.

Carbon coating by CVD. In the last step of Scheme 1, the obtained pSi or pSi/CNT was loaded in a corundum boat and placed at the center of a quartz tube furnace. Then, the precursor gas (argon and toluene) was introduced into the furnace. Next, the furnace temperature was increased from room temperature to 800 °C at a rate of 10 °C min^{-1} and maintained at 800 °C for 20 min. At high temperatures, the toluene decomposed quickly and carbon was deposited onto the surface of the particles. The cooling rate was maintained at 5 °C min^{-1}. The carbon coated pSi and pSi/CNT composites are designated as pSi/C and pSi/CNT/C, respectively, and the carbon contents in the composites are listed in Table 1, which were determined by thermogravimetric (TG) analysis. The whole preparation processes for pSi/C and pSi/CNT/C are illustrated in routes (1) and (2) of Scheme 1, respectively.

For comparison, the silicon powder containing nano- and micro-particles (hereafter abbreviated as cSi) was prepared

Table 1 Carbon types and the weight ratios of the composite samples

	CNT (wt%)	C from CVD (wt%)
pSi/C	0	24.5
pSi/CNT/C	5.2	20.2

from magnesiothermically-reduced commercial nano-SiO_2 (*ca.* 20 nm, Aladdin) under the same conditions, but without the initial spray drying process.

Structure and morphology characterization

The X-ray diffraction (XRD) measurements were carried out using a Rigaku D/MAX-2200/PC X-ray diffractometer at 40 kV and 30 mA with a Cu Kα radiation source. The specific surface area and pore size distribution were determined from the results of the nitrogen adsorption/desorption measurements using an ASAP 2020 accelerated surface area and porosimetry (Micromeritics Inc., USA). The morphologies and microstructures of the samples were investigated using a FEI Nova SEM 230 ultra-high resolution FESEM and a JEM-2100F TEM (JEOL Ltd, Japan). The inductively coupled plasma (ICP) measurements were carried out using an inductively coupled plasma optical emission spectrometer iCAP6300 (ThermoFisher, USA). The carbon contents of the samples were measured by Thermogravimetric Analysis (TGA7, Perkin Elmer, Inc., USA).

Cells assembling and electrochemical tests

The working electrodes were composed of active material, super P conductive carbon black (40 nm, Timical) and styrene butadiene rubber/sodium carboxymethyl cellulose (SBR/SCMC, 1 : 1 by weight) as a binder at a weight ratio of 60 : 20 : 20 with an active material loading of 0.6–0.8 mg cm^{-2} unless otherwise specified. After casting the mixture onto a copper foil and drying, the electrodes were cut to Φ12 mm disks and dried at 80 °C in a vacuum for 4 h.

Coin-type CR 2016 cells were assembled in an argon filled glove box (MBraun, Unilab, Germany) using an ENTEK ET20–26 membrane as a separator and lithium-foil as counter electrode. The oxygen and water contents in the glove box were less than 10 ppm. Unless otherwise specified, the electrolyte was 1 M $LiPF_6$ in a mixed solvent of dimethyl carbonate (DMC) and ethylene carbonate (EC) (1 : 1 by volume) containing 10 vol% fluoroethylene carbonate (FEC). The test cells were charged and discharged at room temperature between 0.01 V and 1.2 V *versus* Li/Li^+ using a commercially available battery test system (LAND CT2001A model, Wuhan Jinnuo Electronics Co., Ltd). The specific capacity was calculated according to the total composite weight.

Results and discussion

SEM and TEM morphologies

Fig. 1 shows the SEM images of the samples from route (1) of Scheme 1. $pSiO_2$/PVA particles with a size of about 10–15 μm were obtained using a spray drying method (Fig. 1a). Most of the $pSiO_2$/PVA particles were hollow with a wall thickness of several micrometers. As shown in Fig. 1b, the PVA acts as a soft template material and homogeneously coheres with the SiO_2 nanoparticles. The SiO_2 nanoparticles with a size of about 15 nm agglomerate to form microparticles. The $pSiO_2$ was obtained after removing the PVA template by calcination at 900 °C for 2 h in air. The calcined SiO_2 particles retain the original morphology (Fig. 1c and d). The SiO_2 nanoparticles were connected and sintered to form a porous structure, and both macropores and nanopores can be observed clearly from Fig. 1d.

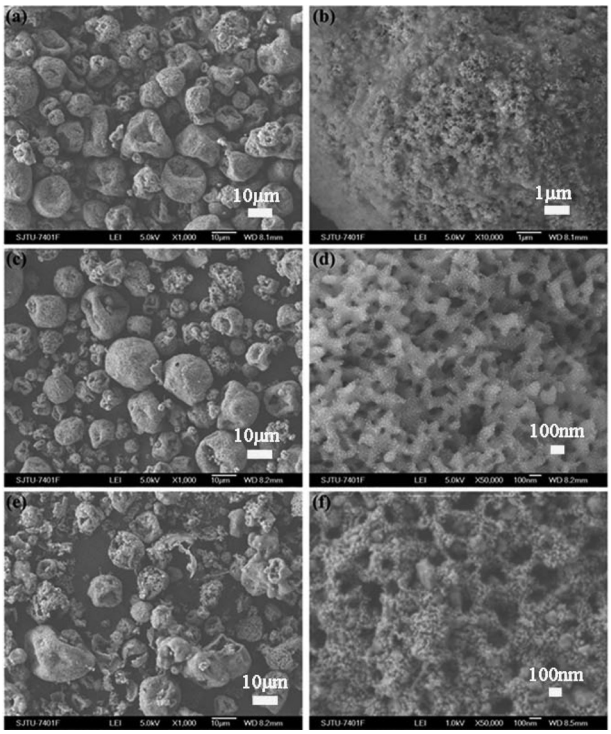

Fig. 1 SEM images of (a, b) SiO_2/PVA after spray drying, (c, d) $pSiO_2$ after calcined at 900 °C for 2 h in air and (e, f) pSi after HCl etching.

The pSi was prepared by the magnesiothermic reduction of the $pSiO_2$, and a part of pSi retains the morphology of the $pSiO_2$ precursor, which serves not only as a template, but also as a silicon source. The pSi particles were constructed by numerous uniform silicon crystallites with sizes of *ca.* 20–30 nm (Fig. 1e and f). The enlarged SEM image of Fig. 1f also confirms the macroporous structure with a size of about 150 nm, which may arise from spray drying. In addition, an insight into the fine structure also reveals the open nanoporous character (Fig. 2b). This was further determined by Brunauer–Emmett–Teller (BET) measurements, which revealed that the specific surface area of the pSi was 60.1 m^2 g^{-1} (Fig. 3a). The abrupt increase in absorbed N_2 at a high relative pressure can be attributed to the adsorption of nitrogen in the macropores. According to the BJH pore diameter distribution in Fig. 3b, the average/mean pore distribution in pSi lies in 29.2 nm with a cumulative pore volume of 0.44 cm^3 g^{-1}.

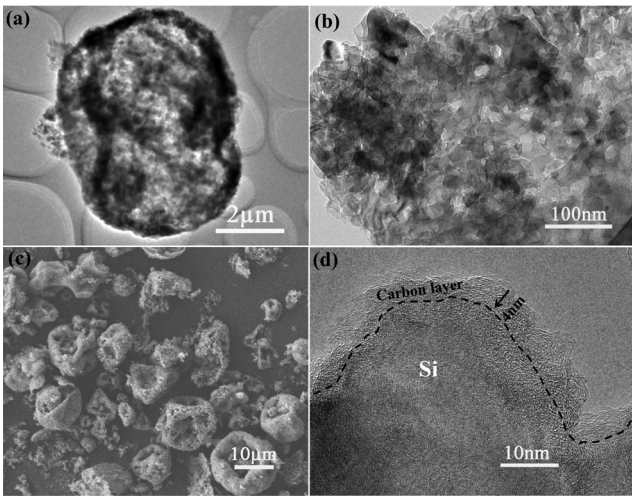

Fig. 2 (a, b) TEM images of pSi, (c) SEM image of pSi/C and (d) HR-TEM image of an interfacial region of pSi/C.

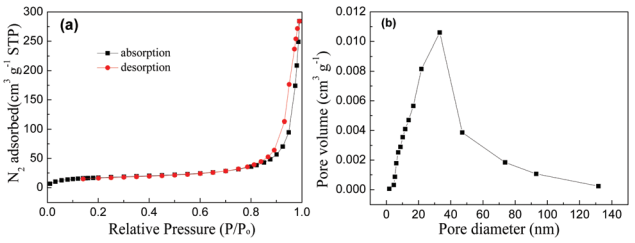

Fig. 3 (a) Nitrogen adsorption–desorption isotherm linear plot and (b) Barrett–Joyner–Halenda (BJH) pore size distribution of the pSi.

The nanopores may result in the $pSiO_2$ template and MgO was completely removed from the composite. Both nanopores and macropores may effectively accommodate the volume changes in silicon and avoid the strong mechanical stress and pulverization during cycling. The pores of the $pSiO_2$ template not only provide the original pores of pSi, but also allow magnesium gas to penetrate into the silica template, which is favorable for the complete conversion of the reactant to form Si nanocrystals without undesirable byproducts, such as Mg_2Si and Mg_2SiO_4. The XRD patterns in Fig. 4a confirm the evolution of phase structures from the $pSiO_2$ to the final product. The crystalline Si phase and MgO were formed after a magnesiothermic reaction and the intermediate product MgO was

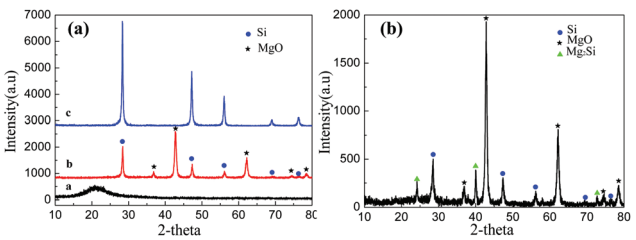

Fig. 4 XRD patterns of (a) the $pSiO_2$, pSi/MgO, pSi and (b) the cSi before HCl etching.

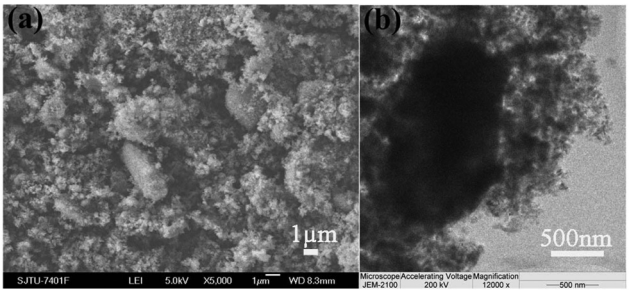

Fig. 5 (a) SEM images and (b) TEM images of cSi.

completely removed by the etching process using a HCl solution. In contrast, the Mg_2Si byproduct is observable in addition to Si and MgO when commercial nano-SiO_2 is directly reduced by a magnesiothermic reaction (Fig. 4b). Moreover, the SEM and TEM images as shown in Fig. 5 reveal that the clumpy silicon in microsizes exists in the cSi powder. The possible reason is that vaporized Mg cannot rapidly infiltrate into the nano-SiO_2 and the local strong heat released from magnesiothermic reduction may agglomerate the as-synthesized silicon domains into large crystals.

In order to improve electronic conductivity of porous silicon and suppress the electrolyte corrosion to Si, carbon is covered on the pSi by CVD method to obtain a pSi/C composite with a carbon content of 24.5 wt%. Fig. 2c and d show the SEM and TEM images of the pSi/C composite. A carbon coating with a thickness of *ca.* 4.0 nm did not change the morphology of pSi and the porous structure was maintained. The pSi/C composite possessed a high specific surface area of 56.8 $m^2\ g^{-1}$, which is favorable for the fast electrode kinetics.

To reinforce the composite structure and enhance the inner electronic conductivity, the MWCNTs were further incorporated into the material according to the same synthetic procedure (route (2) of Scheme 1). As shown in Fig. 6a, the synthesized $pSiO_2$/CNT composite showed a quasi-spherical

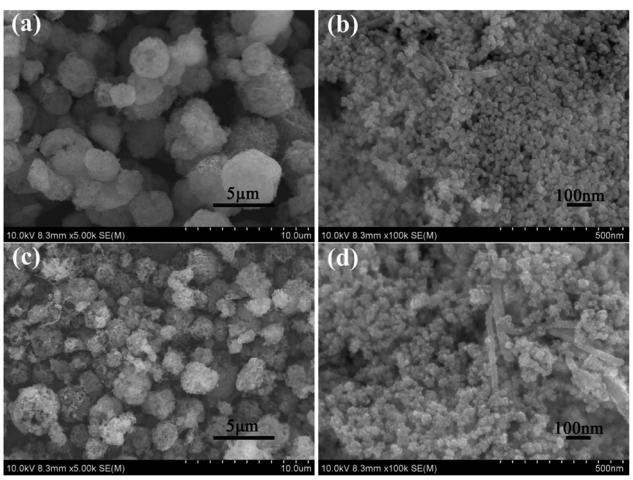

Fig. 6 SEM images of (a, b) $pSiO_2$/CNT after spray drying and (c, d) pSi/CNT after HCl etching.

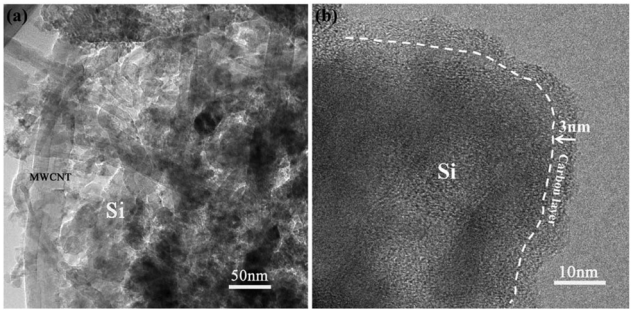

Fig. 7 TEM images of (a) pSi/CNT composite and (b) an interfacial region of silicon/carbon in pSi/CNT/C.

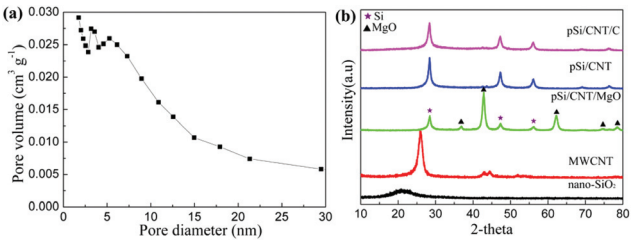

Fig. 8 (a) BJH pore size distribution of the pSi/CNT; (b) XRD patterns of precursors, intermediate and products.

morphology with a particle size from 2 μm to 5 μm. This hierarchical microstructure was constructed by large numbers of uniform nano-SiO_2 with sizes of *ca.* 20 nm distributed in the MWCNT network (Fig. 6b). After, magnesiothermic reduction and etching, the $pSiO_2$/CNT was reduced to pSi/CNT composite. The original second particle configuration was retained and no bulk agglomeration was detected. Although the primary Si crystallites less than 20 nm can be discerned, the interparticle connection was stabilized probably because of a sintering function under thermal reduction (Fig. 6d). The TEM result in Fig. 7 reveals that the Si nanoparticles are homogenously dispersed in a three-dimensional MWCNT conductive network. In addition, irregular nanopores exist in the as-prepared pSi/CNT composite, leading to a large BET surface area of 202 m^2 g^{-1} with a pore volume of 0.633 cm^3 g^{-1}. These values are larger than those of pSi. Moreover, in contrast to pSi, macropores were hardly detected (Fig. 6d) and the smaller nanopores mostly below 5 nm were observed in the pSi/CNT composite (Fig. 8a). After the carbon coating by CVD process, the uniform carbon layer with *ca.* 3 nm was covered on the surface of Si (Fig. 7b).

The nano-SiO_2, MWCNT and different products were characterized using XRD to obtain their structural information. Fig. 8b shows that the nano-SiO_2 has a broad reflection at 25°, indicating its amorphous state. The MWCNT has a strong reflection at 26° and a weak one at 43°, respectively, indicating its graphite-like structure. After the magnesiothermic reaction, the composite exhibited typical reflections of crystalline silicon and MgO. The intermediate product MgO was removed by the etching process using a HCl solution. ICP analysis result indicated that the main impurity in pSi/CNT was still magnesium and its content was about 0.12 wt%. Because of the low MWCNT content (*ca.* 5.2 wt%) and its effective embedding in silicon nanoparticles, the reflection of MWCNT at 25° 2θ was hardly detected for the pSi/CNT/MgO and pSi/CNT composite.

Electrochemical properties

Fig. 9a illustrates the cycling performance of the cSi and pSi in the voltage range of 0.01–1.2 V (*vs.* Li^+/Li). The pSi electrode presented a markedly higher initial capacity of 2871.3 mA h g^{-1} than the cSi (1831.3 mA h g^{-1}). Moreover, 81% of the capacity at the 2nd cycle was retained after 50 cycles for pSi, compared to 36% for cSi. The superior electrochemical performance of pSi can be attributed to the fact that its nanoscale of primary silicon particles prevents fracture during the volume change and the numerous pores offer sufficient space to absorb the huge volume expansion of silicon. For cSi, the large bulk particles may be more responsible for the poor cyclability. This result indicates that the spray drying process benefits the improvement of the electrochemical performance.

Fig. 9b compares the rate performance of pSi, pSi/C and pSi/CNT/C. pSi delivers a higher capacity than pSi/C at a low current rate because of the lack of the less-active carbon (low reversible capacity of *ca.* 150 mA h g^{-1} at 0.3 A g^{-1}). However, its capacity became smaller when the current rate exceeds 1 A g^{-1}. With a further increases in the current rate, the capacity dropped quickly. In contrast, a high reversible capacity of *ca.* 1100 mA h g^{-1} was obtained at a current rate of 5 A g^{-1} for pSi/C. More noticeably, the incorporation of MWCNT into the material further enhanced the rate performance. Its stable and

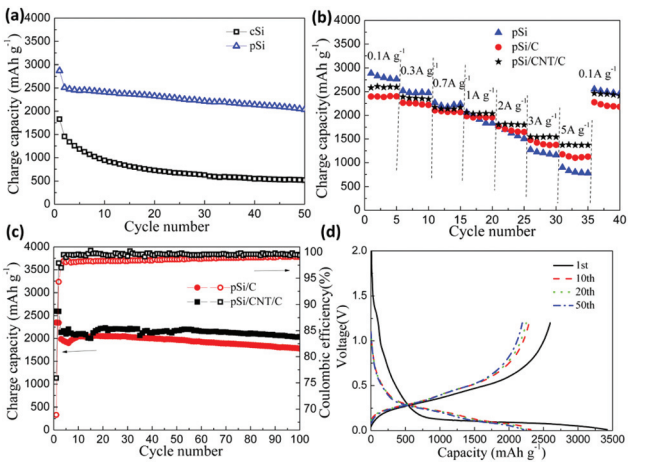

Fig. 9 (a) Cycling performance of the cSi and pSi at a current density of 0.1 A g^{-1} in the initial cycle and at 0.3 A g^{-1} in the following cycles. (b) Reversible capacities of the pSi, pSi/C and pSi/CNT/C composites cycled at different rates from 0.1 to 5 A g^{-1}. (c) Cycling performance and coulombic efficiencies of the pSi/C and pSi/CNT/C samples at a current density of 0.1 A g^{-1} for the initial two cycles and at 1 A g^{-1} in the following cycles. (d) Galvanostatic charge–discharge profiles of the pSi/CNT/C composite for the 1st, 10th, 20th and 50th cycle at a current density of 0.1 A g^{-1} in the initial cycle and at 0.3 A g^{-1} in the following cycles.

reversible capacity reached ~1370 mA h g^{-1} at 5 A g^{-1} and almost full capacity could be recovered (*ca.* 2465 mA h g^{-1}) when the current rate was returned to 0.1 A g^{-1}. Comparing the three samples, it was noted that the cycle capacity is dominated by the Si content in the composite below 0.7 A g^{-1} because the carbon contributes a very lower capacity. At a higher rate, the kinetic factor is dominant. The porous nano/micro-structure alone is not enough to maintain the rapid electrode kinetics because of its low electronic conductivity and a multi-dimensional carbon modification is effective for capacity retention at a high rate.

The long cycling behaviour of the pSi/C and pSi/CNT/C composites in the voltage range of 0.01–1.2 V (*vs.* Li^+/Li) at 1 A g^{-1} (0.1 A g^{-1} in the initial two cycles for electrode activation) is shown in Fig. 9c. The pSi/C electrode delivered a reversible capacity of 1986.3 mA h g^{-1} in the 3rd cycle and 1780.4 mA h g^{-1} after 100 cycles with the capacity retention of 90%. After 60 cycles, the coulombic efficiency increased to 99%. The addition of MWCNT with 5.2 wt% into the composite greatly improved the electrochemical reversibility and its capacity of 95.5% could be maintained under the same conditions. In addition, its coulombic efficiency quickly increased to 99% after the initial several cycles. The improvement in the cyclability can be attributed to the following reasons: (1) The MWCNT constructs a highly conductive network and stabilizes the porous composite configuration; (2) the sufficient void space allows the silicon to expand without changing the secondary particle size; and (3) the uniform thin surface carbon layer reinforces the conducting network and may also prevent the aggregation of Si nanoparticles during repeated cycles.

Fig. 9d presents the voltage profiles of the pSi/C composite for the 1st, 10th, 20th and 50th cycle. The first discharge and charge capacities are 3422.5 and 2596.6 mA h g^{-1} with a coulombic efficiency of 75.9%. The irreversible capacity loss could originate from the formation of the SEI film and irreversible lithiation of structure defects in the active phases, including MWCNT, which may overcome by prelithiating the electrode.[34,35] Additionally, the first discharge curve displays a long flat plateau below 0.1 V, which is attributed to the Li-insertion of crystalline Si to form an amorphous Li_xSi phase. Next, the discharge and charge curves show the stable characteristic of amorphous Si with a reversible capacity around 2300 mA h g^{-1}.

The effects of the loading density of the active material in electrode and FEC electrolyte additive on the electrochemical behavior were further examined. Here, the pSi/CNT/C electrode composition (active material : Super P : SBR/SCMC) was adjusted from 60 : 20 : 20 to 80 : 10 : 10 with the same electrode thickness. As shown in Fig. 10, the initial discharge and charge capacity in the FEC-free electrolyte were 3101.8 mA h g^{-1} and 2495.8 mA h g^{-1}, with a coulombic efficiency of 80.5%. After 60 cycles, its charge capacity was 712.6 mA h g^{-1}, retaining 34% of the 3rd cycle capacity. By contrast, the cycling performance can be significantly enhanced in a FEC-containing electrolyte. A similar effect and the related discussion have been reported.[36,37] On the other hand, after comparing with

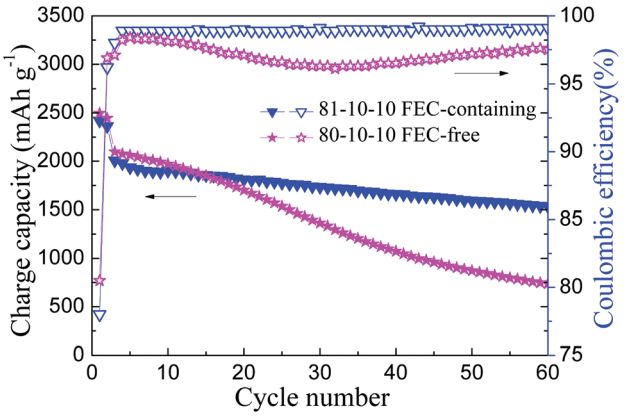

Fig. 10 Cycling behaviors and coulombic efficiencies of the pSi/CNT/C electrode with a composition of 80 wt% pSi/CNT/C, 10 wt% Super P, and 10 wt% SBR/SMC in FEC-free and FEC-containing electrolytes at a current density of 0.1 A g^{-1} for the initial two cycles and at 1 A g^{-1} in the following cycles.

Fig. 9c, the higher loading leads to a faster capacity fading during cycling. It appears that the volume effect of the active material is responsible for this.

The interfacial property between the electrode and electrolyte was examined by AC impedance measurements. Fig. 11 shows Nyquist plots of the cSi, pSi, pSi/C and pSi/CNT/C electrodes at 1.2 V after 10 cycles. The cSi and pSi electrodes exhibit Nyquist plots consisting of two depressed semicircles in the high-middle frequency region and an oblique straight line in the low frequency region. The measured impedance data over the entire frequency range was analyzed using the inset equivalent circuit in Fig. 12. The first semicircle implies the resistance through the SEI film (R_f) and the second one is related to the charge transfer resistance at the electrode–electrolyte interface (R_{ct}). The oblique straight line corresponds to the ion diffusion kinetics.[38] Unlike the uncoated composite electrodes, only a single oblate semicircle can be observed for

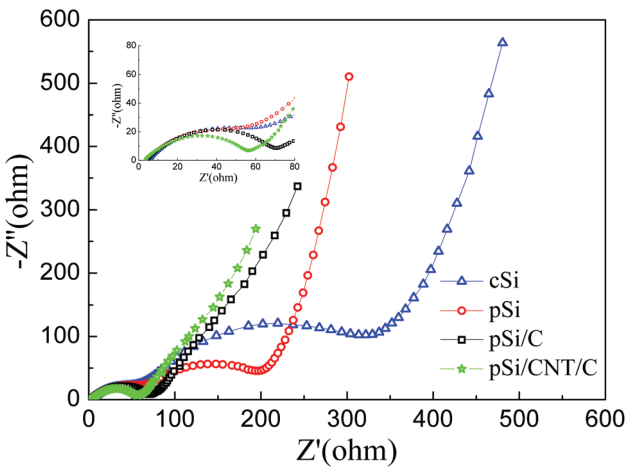

Fig. 11 Nyquist plots of the cSi, pSi, pSi/C and pSi/CNT/C electrodes after the cycling tests. Inset is the close-up of the resistance (Z') range between 0 and 80 ohms.

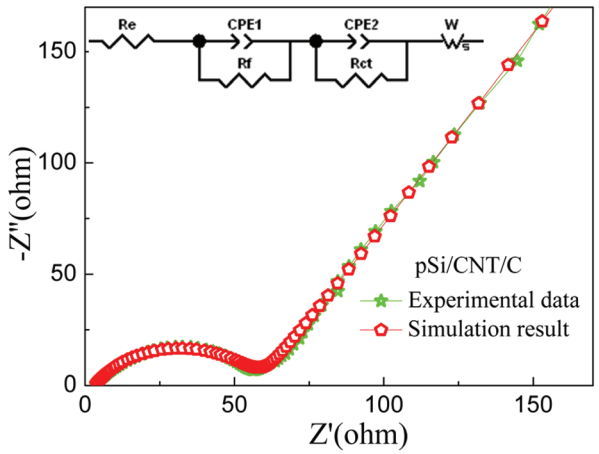

Fig. 12 Nyquist plot of the pSi/CNT/C electrode after the cycling test and its simulation result using the inset equivalent circuit.

the composites after modification with carbon. This oblate semicircle may include whole resistance from the SEI film to the interfacial charge-transfer. Coating a carbon nanolayer on the particle surface makes the interfacial resistance in the high-middle frequency range evidently smaller. In particular, the hierarchical pSi/CNT/C electrode presents the smallest high-middle frequency semicircle, which could be because of the reliable electronic connection of the active Si nanoparticles *via* the highly conductive MWCNT network. The simulated impedance spectra and the experimental EIS data are shown in Fig. 12. The relative standard deviations for most parameters obtained from fitting the experimental impedance spectra were less than 2%, which indicates that the proposed model can describe the experimental result satisfactorily. For cSi, the especially large charge-transfer resistance (249 Ω) may be related to the instability of the electrode structure during cycling.

The morphological evolution of the pSi/CNT/C particles during cycling was verified by SEM characterization (Fig. 13).

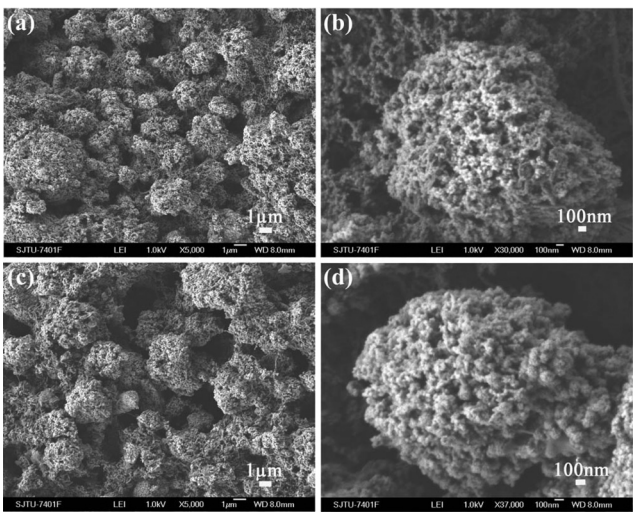

Fig. 13 SEM images of the pSi/CNT/C electrodes before cycling (a, b) and after 100 cycles at a current density of 1 A g^{-1} (c, d).

After 100 cycles, the Si nanoparticle size obviously increases mainly because of the irreversible volume expansion caused by lithium insertion (Fig. 13d). However, the initial quasi-spherical morphology remains, indicating its structural integrity and steadiness over the repeated charge and discharge (Fig. 13c).

Conclusions

Novel nano/micro-structured pSi and pSi/CNT were successfully synthesized using cheap nano-SiO_2 as the silicon source and further covered with nano-layered carbon for high performance anode material in lithium ion batteries. The unique hierarchical secondary particles and porous structure can effectively accommodate the volume changes of Si during cycling and provide a large interfacial reaction zone, while the uniform thin carbon layer ensures high electronic conductivity of the electrode. In particular, MWCNT reinforces the composite structure and enhances the inner electronic conductivity. Thus, the electrochemical performance of the composite is greatly improved. The pSi/CNT/C composite exhibits a high reversible capacity of *ca.* 2100 mA h g^{-1} and excellent cycling stability at a current rate of 1 A g^{-1}. Furthermore, it also maintains the reversible capacity of *ca.* 1370 mA h g^{-1} even at high current rate of 5 A g^{-1}. The facile synthesis technique and the superior electrochemical performance make this composite a promising candidate for next-generation large capacity and high power lithium ion battery anode material. More investigation should be done towards a higher loading density of the active materials for practical applications.

Acknowledgements

This work is supported by State Key Basic Research Program of the PRC (no. 2014CB932303) and SJTU-UM jointed research project.

Notes and references

1 H. K. Liu, Z. P. Guo, J. Z. Wang and K. Konstantinov, *J. Mater. Chem.*, 2010, **20**, 10055–10057.
2 S. Sim, P. Oh, S. Park and J. Cho, *Adv. Mater.*, 2013, **25**, 4498–4503.
3 S. Iwamura, H. Nishihara and T. Kyotani, *J. Power Sources*, 2013, **222**, 400–409.
4 J. R. Szczech and S. Jin, *Energy Environ. Sci.*, 2011, **4**, 56–72.
5 M. Ge, X. Fang, J. Rong and C. Zhou, *Nanotechnology*, 2013, **24**, 422001–422010.
6 W. Wang and P. N. Kumta, *ACS Nano*, 2010, **4**, 2233–2241.
7 H. Jia, P. Gao, J. Yang, J. Wang, Y. Nuli and Z. Yang, *Adv. Energy Mater.*, 2011, **1**, 1036–1039.
8 H. Tao, L.-Z. Fan, W.-L. Song, M. Wu, X. He and X. Qu, *Nanoscale*, 2014, **6**, 3138–3142.
9 Y. Chen, S. Zeng, J. Qian, Y. Wang, Y. Cao, H. Yang and X. Ai, *ACS Appl. Mater. Interfaces*, 2014, **6**, 3508–3512.

10 K. Fu, Y. Lu, M. Dirican, C. Chen, M. Yanilmaz, Q. Shi, P. D. Bradford and X. Zhang, *Nanoscale*, 2014, **6**, 7489–7495.
11 J. Cho, *J. Mater. Chem.*, 2010, **20**, 4009–4010.
12 D. Chen, X. Mei, G. Ji, M. Lu, J. Xie, J. Lu and J. Y. Lee, *Angew. Chem., Int. Ed.*, 2012, **51**, 2409–2413.
13 M. Thakur, R. B. Pernites, N. Nitta, M. Isaacson, S. L. Sinsabaugh, M. S. Wong and S. L. Biswal, *Chem. Mater.*, 2012, **24**, 2998–3003.
14 Y. Yu, L. Gu, C. Zhu, S. Tsukimoto, P. A. van Aken and J. Maier, *Adv. Mater.*, 2010, **22**, 2247–2250.
15 X. Li and L. Zhi, *Nanoscale*, 2013, **5**, 8864–8873.
16 M. Ge, X. Fang, J. Rong and C. Zhou, *Nanotechnology*, 2013, **24**, 422001–422010.
17 M. Ge, J. Rong, X. Fang and C. Zhou, *Nano Lett.*, 2012, **12**, 2318–2323.
18 H. Kim, B. Han, J. Choo and J. Cho, *Angew. Chem., Int. Ed.*, 2008, **47**, 10151–10154.
19 N. Liu, K. Huo, M. T. McDowell, J. Zhao and Y. Cui, *Sci. Rep.*, 2013, **3**, 1919–1925.
20 L. Shen, X. Guo, X. Fang, Z. Wang and L. Chen, *J. Power Sources*, 2012, **213**, 229–232.
21 Y. Hwa, W.-S. Kim, B.-C. Yu, S.-H. Hong and H.-J. Sohn, *Energy Technol.*, 2013, **1**, 327–331.
22 N. Dimov, S. Kugino and M. Yoshio, *J. Power Sources*, 2004, **136**, 108–114.
23 B. Fuchsbichler, C. Stangl, H. Kren, F. Uhlig and S. Koller, *J. Power Sources*, 2011, **196**, 2889–2892.
24 X. Li, J.-H. Cho, N. Li, Y. Zhang, D. Williams, S. A. Dayeh and S. T. Picraux, *Adv. Energy Mater.*, 2012, **2**, 87–93.
25 Y.-S. He, P. Gao, J. Chen, X. Yang, X.-Z. Liao, J. Yang and Z.-F. Ma, *RSC Adv.*, 2011, **1**, 958–960.
26 D. P. Wong, H.-P. Tseng, Y.-T. Chen, B.-J. Hwang, L.-C. Chen and K.-H. Chen, *Carbon*, 2013, **63**, 397–403.
27 Y. Wen, Y. Zhu, A. Langrock, A. Manivannan, S. H. Ehrman and C. Wang, *Small*, 2013, **9**, 2810–2816.
28 Y.-S. Ye, X.-L. Xie, J. Rick, F.-C. Chang and B.-J. Hwang, *J. Power Sources*, 2014, **247**, 991–998.
29 X.-M. Liu, Z. D. Huang, S. W. Oh, B. Zhang, P.-C. Ma, M. M. F. Yuen and J.-K. Kim, *Compos. Sci. Technol.*, 2012, **72**, 121–144.
30 C. de las Casas and W. Li, *J. Power Sources*, 2012, **208**, 74–85.
31 C. Martin, O. Crosnier, R. Retoux, D. Bélanger, D. M. Schleich and T. Brousse, *Adv. Funct. Mater.*, 2011, **21**, 3524–3530.
32 P. Gao, Y. Nuli, Y.-S. He, J. Wang, A. I. Minett, J. Yang and J. Chen, *Chem. Commun.*, 2010, **46**, 9149–9151.
33 A. Gohier, B. Laïk, K.-H. Kim, J.-L. Maurice, J.-P. Pereira-Ramos, C. S. Cojocaru and P. T. Van, *Adv. Mater.*, 2012, **24**, 2592–2597.
34 Y. Li and B. Fitch, *Electrochem. Commun.*, 2011, **13**, 664–667.
35 W. Seong II and W. Y. Yoon, *J. Power Sources*, 2010, **195**, 6143–6147.
36 V. Etacheri, O. Haik, Y. Goffer, G. A. Roberts, I. C. Stefan, R. Fasching and D. Aurbach, *Langmuir*, 2012, **28**, 965–976.
37 Y.-M. Lin, K. C. Klavetter, P. R. Abel, N. C. Davy, J. L. Snider, A. Heller and C. B. Mullins, *Chem. Commun.*, 2012, **48**, 7268–7270.
38 J. Guo, A. Sun, X. Chen, C. Wang and A. Manivannan, *Electrochim. Acta*, 2011, **56**, 3981–3987.